Applied Surface Science Advances 33 (2026) 100965

Contents lists available at ScienceDirect

Applied Surface Science Advances

journal homepage: www.sciencedirect.com/journal/applied-surface-science-advances

Full Length Article

Stabilization of isolated Fe atoms on a 1-nm-thick MgO/Fe(001) insulating surface via critical tunneling for a robust quantum spin platform

Toyo Kazu Yamada [a,b,*], Nana K.M. Nazriq [a], Kohei Tada [c,d]

[a] Department of Materials Science, Chiba University, 1-33 Yayoi-Cho, Inage-ku, Chiba 263-8522, Japan
[b] Molecular Chirality Research Centre, Chiba University, 1-33 Yayoi-cho, Inage-ku, Chiba 263-8522, Japan
[c] Department of Materials Engineering Science, Graduate School of Engineering Science, The University of Osaka, Toyonaka 560-8531, Osaka, Japan
[d] Innovative Catalysis Science Division, Institute for Open and Transdisciplinary Research Initiatives (ICS-OTRI), The University of Osaka, Suita 565-0871, Osaka, Japan

ARTICLE INFO

Keywords:
Quantum spin
STM
Atom
MgO
iron

ABSTRACT

Atomically flat insulating films are essential for decoupling adsorbates from metallic substrates and preserving the intrinsic electronic and spin properties of single-atom quantum bits (qubits). Here, we show that the widely used MgO/Fe(001) spintronic system provides a robust platform for single-atom qubits. Using scanning tunneling microscopy (STM) at 4.6 K under ultrahigh vacuum, we investigate ~1-nm-thick MgO films exhibiting high crystalline quality, a well-defined band gap, and a low defect density. Single Fe atoms deposited on this surface form a double-barrier tunneling junction between vacuum and MgO, with Fe(001) and the STM tip acting as electrodes.

In contrast to the commonly studied bilayer MgO films on noble-metal substrates, the increased thickness of MgO on Fe(001) renders STM imaging highly challenging, as the MgO thickness is comparable to the tip–sample separation and imaging near the band gap readily induces adatom displacement. We identify a narrow critical tunneling regime that enables stable imaging, revealing that Fe adatoms are strongly stabilized on the MgO surface. Density functional theory calculations show that crystal and ligand fields lift the orbital degeneracy of Fe, leading to cationic Fe atoms with an effective spin $S \approx 3/2$ and strong bonding to surface oxygen atoms.

1. Introduction

Isolated single atoms possess discrete orbitals, allowing their spin states to be tuned for qubit control [1–3]. However, when these atoms are adsorbed on solid surfaces, serving as substrates for qubit device applications [4–7], their spins experience various interactions. In particular, when atoms are in contact with metallic surfaces, a single atomic spin can be screened by conduction electrons through antiferromagnetic coupling, resulting in a zero-bias peak or Kondo resonance [8–10]. While this feature confirms the presence of a surface spin, the screening effect suppresses direct access to it. Furthermore, inelastic electron scattering can induce spin flips [5–12], thereby reducing spin lifetimes.

To mitigate these effects, atomically thin insulating monolayers such as Al_2O_3 [13], MgO [14–16], NaCl [17,18], or Cu_2N [19,20] have gained significant attention. These layers effectively decouple adsorbed atoms from the conduction electrons of the metallic substrate, thereby preserving their spin states. This not only activates the intrinsic functionalities of the atoms but also allows the local crystal and ligand fields of the insulator to modulate atomic orbital alignments. Thus, engineering ultrathin insulating films as protective and supportive templates for adsorbed quantum nanomaterials opens new avenues for developing atomic qubits [4,7], molecular magnet qubits [11,21–23], and even enabling molecular motion functionalities [24,25].

Although such electronic decoupling might suggest weak interactions between the adsorbed atoms and the insulating surface, this is not necessarily the case. In fact, the interaction strength strongly depends on orbital hybridization, which is modified as the degeneracy of gas-phase orbitals is lifted by local crystal and ligand fields. This process often induces charge transfer, causing the adsorbed atoms to become ionized [7,14,26–31].

Scanning tunneling microscopy (STM) is a powerful technique for imaging and manipulating single atoms adsorbed on solid surfaces. Atomic-scale experiments have been successfully performed not only on metallic surfaces [32,33] but also on insulating surfaces [7,29,34]. This is because the insulating surface provides much higher tunneling

* Corresponding author.
E-mail address: toyoyamada@faculty.chiba-u.jp (T.K. Yamada).

https://doi.org/10.1016/j.apsadv.2026.100965
Received 11 December 2025; Received in revised form 8 February 2026; Accepted 2 March 2026
Available online 10 March 2026
2666-5239/© 2026 The Authors. Published by Elsevier B.V. This is an open access article under the CC BY license (http://creativecommons.org/licenses/by/4.0/).

resistance and therefore enhances local forces and electric fields, applying from the tip to the atom, which can easily induce atomic motion, making stable imaging challenging. Nonetheless, STM investigations on insulating films are crucial for single-atom quantum devices, as they reveal how atomic positions, local crystal fields, and the resulting hybridization between discrete atomic orbitals and the surface density of states modify charge transfer and consequently influence quantum spin states. In other words, engineering robust quantum spin states requires stabilization of the atoms within a double-insulating-barrier configuration. This single-atom double-barrier tunnel junction is essential for accessing and controlling the electronic spin states of individual atoms through the tunneling gap and serves as a fundamental model for qubit systems, particularly when combined with microwave excitations [21–35].

Another key factor is the thickness of the insulating film. To date, monolayer or bilayer insulating films epitaxially grown on noble-metal substrates have been predominantly used [29,31,36–38]. These films, typically 0.2–0.4 nm thick, are suitable for fundamental studies; however, in practical applications, films are often fabricated by sputtering [39–42], which makes it difficult to produce defect-free ultrathin layers. Therefore, a minimum thickness of approximately 1 nm is desirable.

In this study, we employed the widely used spintronic system MgO/Fe(001) [39–42] with an MgO thickness of approximately 1 nm [15,16], corresponding to four monolayers, using our home-built STM operated under ultrahigh vacuum at 4.6 K [43].

It should be noted that the use of an insulating film that is nearly twice as thick as a bilayer film leads to critical differences in STM observations on MgO surfaces. Most previous STM studies have been conducted on bilayer MgO films with a thickness of approximately 0.4 nm. In such systems, when the STM probes the surface within the MgO band gap near the Fermi energy and assuming an initial tip–sample separation of ~1 nm, the tip approaches the surface by about 0.4 nm. This results in an effective tip–sample separation of ~0.6 nm, which allows conventional STM imaging of atoms on bilayer MgO films. In contrast, the present study is performed on a substantially thicker MgO film with a thickness of ~1 nm, more than twice that of a bilayer film. Under tunneling conditions within the MgO band gap, the STM tip can approach the surface by up to ~1 nm, corresponding to a typical tip–sample separation and effectively near-contact conditions. This significantly increases the difficulty of maintaining immobile adatoms on the MgO surface during STM measurements.

2. Methods

2.1. Home-built low-temperature UHV STM setup

The experiment was performed with a home-built low-temperature STM at 4.6 K under UHV [43]. The setup consists of the introduction, preparation, and analytical chambers with the base pressure below 10^{-8} Pa. A UHV cryostat (CryoVac), including an outer liquid nitrogen tank (8 liters) and inner helium tank (4 liters), is docked in the analytical chamber. The STM was placed at the center of the analytical chamber and thermally contacted with the cryostat. Heat radiation from the analytical chamber to the STM was cut with two cylindrical cooling shields, which maintained the STM temperature of 5 K for 40 h using 4 liters of liquid helium.

2.2. STM / STS measurements

STM and scanning tunneling spectroscopy (STS) measurements were performed with a combined Nanonis SPM controller and software. The topographic images were obtained in a constant current mode. STS was done by measuring tunneling current as a function sample bias voltage (I (V)) at each pixel position in an STM topographic image (feedback-off grid mode). Differential conductance (dI/dV) curves, which are proportional to the sample local density of states (LDOS), were obtained using WSxM 5.0 Develop 10.0 software [44]. via numerical differentiation of $I(V)$ by the sample bias voltage (V).

2.3. Fabrication of W tip

STM tips were fabricated from polycrystalline W and Mo wires with a diameter of 0.3 mm (purity 99.95 %) via electrochemical etching using KOH aq [45], the flame-etching process [46,47], and subsequently transferred into the UHV preparation chamber. Then, the tip apex was flashed at 2000 K to exclude oxide layers [45]. The cleaned tip was again transferred to the UHV analytical chamber without breaking UHV and set into the STM using a wobble stick. The tip was approached on a target Fe atom to apply an electric field. Because of a narrow separation of 0.5–1.0 nm between tip and sample in the STM setup, a tip-sample bias of 1 V produces a large local electric field of 1–2 × 10^9 V/m. The atomically sharp tip apex can apply an electric field within 0.5 nm below the tip apex [48,49], which limits the electric field to a single Fe atom on the MgO surface.

2.4. Ultrathin MgO films on Fe(001)-p(1×1)O

Fe(001) single-crystal whiskers, grown by chemical vapor deposition and containing extremely low impurity concentrations, were used as substrates [16,50,51]. The whiskers have typical dimensions of approximately 1 mm × 1 mm in cross section and about 10 mm in length. They grow along the ⟨100⟩ direction; consequently, all six faces correspond to bcc (001) planes. Owing to their high crystalline quality, these whisker crystals have been extensively employed as ideal ferromagnetic substrates in spin-polarized STM studies [16,50,52–54]. The Fe(001) whisker surface was cleaned through repeated cycles of Ar^+ sputtering (+0.8 kV, +0.80 μA) at 820 K. The cleaned surface was examined using STM/STS, which revealed atomically flat terraces with widths ranging from 50 to 100 nm and the Fe(001) 3d surface state peak at +0.2 eV in the dI/dV curves [50,52,55–57]. Low energy electron diffraction (LEED) patterns confirmed the bcc(001) four-fold symmetry. The Fe(001)-p(1 × 1)O surface was prepared in the preparation chamber by exposing the clean Fe(001) surface to oxygen gas for about 2 Langmuir (60 s, 4.0 × 10^{-6} Pa) while maintaining the substrate temperature at 300 K. STM topographic images showed a clear p(1 × 1) structure, with dark spots corresponding to the positions of oxygen atoms [58–60]. This oxygen monolayer coating prevents further oxidation and interface roughening. The Fe(001)-p(1 × 1)O surface was then re-exposed to oxygen gas (60 s, 1.0 × 10^{-6} Pa) in the preparation chamber, followed by Mg atom deposition from an evaporator (AEV-3, AVC Co., Ltd.) at a sample temperature of 750 K. STM images revealed the growth of atomically flat, ultrathin, square-shaped nanoislands with a terrace width of approximately 40 nm and a uniform height of about 1 nm. Fe (001)-p(1 × 1)O terraces were still visible between the islands [16].

2.5. Fe singles atom deposition

The MgO / Fe(001)-p(1 × 1)O was first cooled down to ~100 K by setting at the cooling stage for 15 min, and second, the sample was put inside the STM sample stage while maintaining the temperature of 5 K for at least 3 h. This avoided unnecessary thermal drift during approach and scanning. Fe atoms were deposited from the Fe evaporator (AEV-11, AVC Co., Ltd.), which points directly to the STM sample stage. The Fe atom deposition was performed by opening the cooling shield shortly (a few seconds), maintaining the sample temperature below 20 K.

2.6. DFT calculations

Electron density and total energy were optimized via self-consistent field (SCF) calculation with the Kohn-Sham equation [61]. The used exchange-correlation function is the Perdew-Burke-Ernzerhof formula in generalized gradient approximation (GGA-PBE) [62]. A plane-wave

basis was used, and the core region was treated by the projector-augmented wavefunction (PAW) method [63,64]. The calculated numbers of valence electrons of Fe, Mg, and O were 8, 2, and 6, respectively. Energy cut-offs were 500 eV (wavefunction) and 2400 eV (augmented charge). The threshold for convergence of energy is 10^{-6} eV for SCF calculation and 10^{-5} eV for geometry optimization. The calculated slab model is a 2 × 2 unit with a vacuum region of 2 nm. The thickness of Fe and MgO are four atomic layers. The specific lattice constants and atomic coordinates are shown in Supplementary Materials, Tables S1 and S2. The bottom layer of Fe was fixed to mimic the bulk structure. A Γ-centred 5 × 5 × 1 mesh was used for *k*-points sampling. For the DFT calculations, VASP programme were used [65–68]. The electron and spin density distributions were visualized by the VESTA programme [69]. Atomic charges were estimated by the Bader algorithm [70–73].

3. Results and discussion

3.1. Critical tunneling conditions to stabilize Fe atoms on MgO/Fe(001)-p (1 × 1)O surface

Imaging transition-metal Fe atoms on insulating surfaces by STM becomes particularly challenging when the thickness of the insulating film (~1 nm) is comparable to the typical tip–sample separation. In this configuration, tunneling electrons from the metallic STM tip must first traverse the vacuum barrier to reach the discrete Fe 3*d* orbitals, and subsequently tunnel from these orbitals through the insulating film into the Fe(001) substrate electrode. A key characteristic of the tunneling conditions is a pronounced reduction in the apparent height of the MgO film, from ~1 nm to ~0.2 nm [15,16], as the bias approaches the band-gap region, depending on the sample bias voltage (V_s) under constant-current feedback. As a result, the STM tip apex can approach sufficiently close to Fe atoms near the MgO band-gap energy, which may lead to the displacement of Fe adatoms from the MgO surface. Therefore,

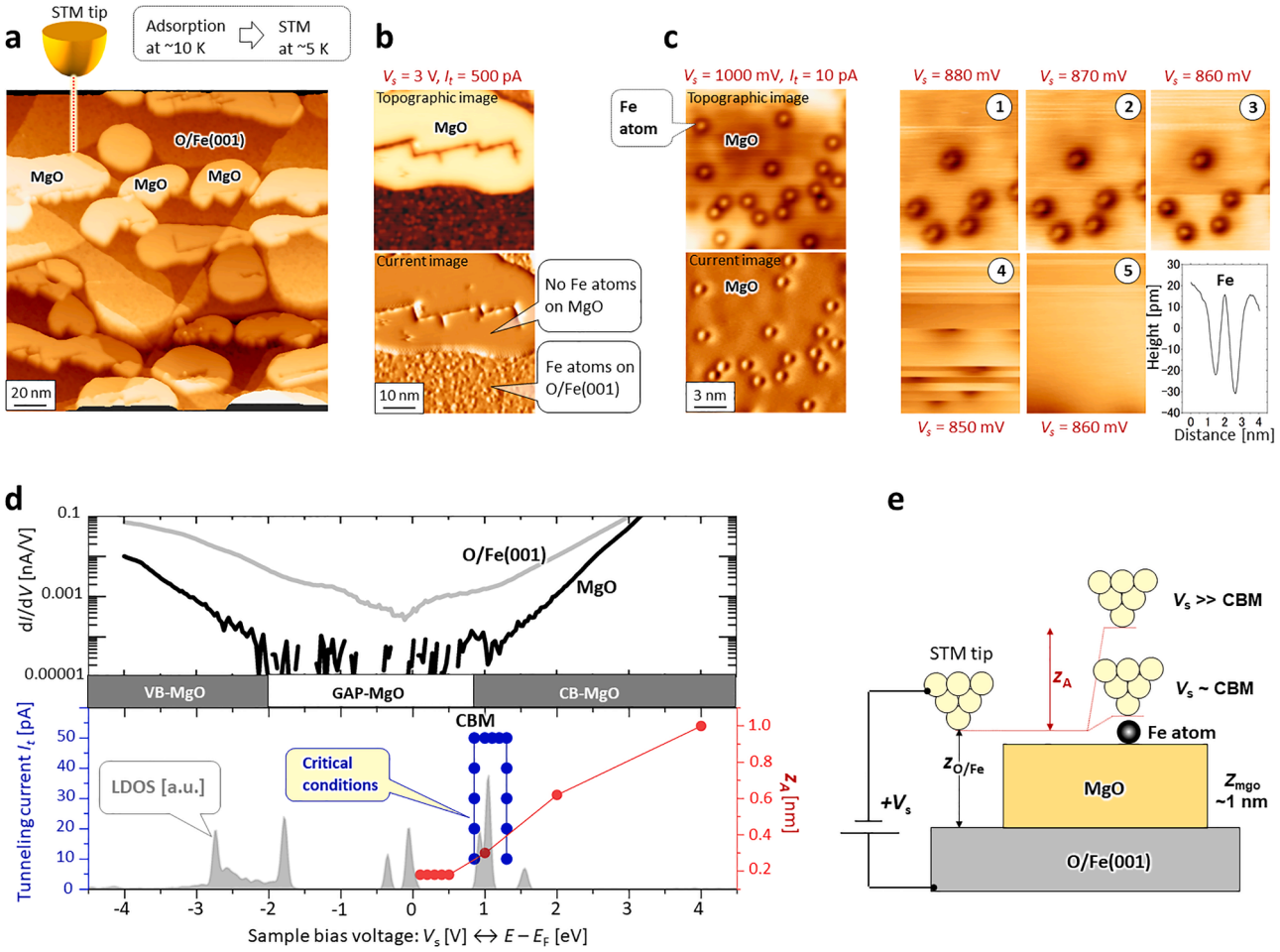

Fig. 1. Limited tunneling conditions for imaging Fe atoms on the MgO/Fe(001)-p(1 × 1)O surface. (a) STM imaging of 1-nm-high MgO islands grown on oxygen-covered Fe(001) substrate terraces (200 × 200 nm^2, V_s = +3.0 V, I_t = 50 pA). (b) STM images (50 × 50 nm^2, V_s = +3.0 V, I_t = 500 pA) acquired on the MgO surface after Fe atom adsorption. The upper and lower panels show the topographic and current images, respectively. (c) Left panels: STM topographic and current images of Fe adatoms on MgO/Fe(001) acquired at V_s = +1000 mV and 10 pA. Right panels: a series of STM topographic images acquired at V_s= 880, 870, 860, 850, and 860 mV (10 × 7 nm^2, I_t = 10 pA). The lower-right panel shows the height profile taken across an Fe atom. (d) Top panel: d*I*/d*V* spectra, proportional to the LDOS, measured on the O/Fe(001) (gray) and MgO (black) surfaces. The O/Fe surface exhibits metallic behavior, while the MgO surface shows insulating properties with a band gap of approximately 3 eV. The valence band maximum (VBM) and conduction band minimum (CBM) are located at around –2 eV and +0.9 eV relative to the Fermi level (V_s = 0 V). Bottom panel: Fe atoms on the MgO surface are visible only under limited tunneling conditions (V_s = 0.85–1.30 V and I_t < 50 pA). Red, blue, and gray markers represent, respectively, the bias-dependent variation in the apparent height of the MgO island (z_A, in nm), the threshold tunneling current that induces atomic displacement, and the discrete local density of states (LDOS) of Fe atoms on MgO calculated by DFT. (e) Schematic spherical model of the STM tip scanning above a single Fe atom on MgO/Fe(001)-p(1 × 1)O. Here, z_A, $z_{O/Fe}$, and zmgo denote the apparent height of the MgO island, the distance between the tip apex and the O/Fe substrate, and the MgO film thickness (~1 nm), respectively.

establishing stable imaging conditions is crucial for the development of robust single-atom–based qubits protected by double insulating barriers on solid surfaces, while maintaining tunneling access to the atomic spin states.

Fig. 1a shows a three-dimensional STM topographic image (200 × 200 nm^2) of atomically-flat MgO nanoislands on an Fe(001) whisker substrate precovered with a one-monolayer oxygen p(1 × 1) film. This oxygen layer suppresses strong direct interactions between MgO and the Fe substrate and limits long-range thermal diffusion during growth, resulting in the formation of MgO nanoislands with lateral sizes of 20–50 nm [16]. The MgO growth was carefully controlled by calibrating the Mg deposition amount using a quartz crystal microbalance in combination with STM imaging, enabling precise evaluation of the deposited coverage. It is well established that thin MgO films grown on metallic substrates exhibit a reduced band gap of approximately 3 eV [16], significantly smaller than the bulk MgO band gap of 7.8 eV [74,75]. In the present system (Fig. 1d), the conduction band minimum (CBM) and valence band maximum (VBM) are located at approximately +850 meV and −2000 meV, respectively.

Single Fe atoms were deposited onto the atomically flat MgO nanoisland terrace. The deposition was performed under ultrahigh vacuum at approximately 10 K by briefly (10 s) opening the cooling shield door inside the STM chamber. Subsequent STM measurements were carried out at 4.6 K. Fig. 1b shows STM images acquired at a sample bias of V_s = +3 V and a tunneling current of I_t = 500 pA, well above the MgO band-gap region. The upper panel presents a topographic STM image, in which both the MgO islands and the Fe(001) substrate surface are clearly resolved. On the MgO island surfaces, only a few dark features are observed, and no Fe atoms are detected, whereas numerous bright protrusions corresponding to Fe atoms are visible on the substrate surface. This contrast is more clearly revealed in the current image shown in the lower panel. The MgO surface appears flat, while many atomic-scale features are present on the substrate. At first glance, these observations might suggest that Fe atoms do not adsorb on the MgO/Fe(001) surface. However, this interpretation is incorrect. In fact, Fe atoms are stably adsorbed on the MgO surface but can be displaced or swept away by the STM tip during imaging.

The left panels of Fig. 1c show STM topographic and current images of single Fe atoms on the MgO surface, acquired at a sample bias of V_s = +1000 mV and a tunneling current of I_t = 10 pA, surprisingly close to the MgO band-gap energy. Under this limited bias condition, we successfully imaged Fe atoms on the MgO/Fe(001) surface. In the topographic image, the Fe atoms appear as dark ring-like features, while in the corresponding current image they are observed as bright dots. Such features were never observed prior to Fe deposition, indicating that these dark ring-like structures are most likely associated with Fe adatoms adsorbed on the MgO surface. One might alternatively consider whether these features could be attributed to atomic-scale defects within the MgO nanoislands. However, prior to Fe deposition, we had carefully identified intrinsic atomic-scale defects on MgO nanoislands [15]. These defects exhibit a distinct LDOS compared to the surrounding MgO and typically appear as isolated dark spots, rather than ring-like features, in STM topographic images, with only a few such defects present on each nanoisland. Moreover, these intrinsic defects appear as bright spots in STS maps and remain stable as a function of bias voltage. They are observable within the MgO band gap, indicating that they are located beneath the surface [15].

Similar ring-like contrasts have frequently been reported for metal adatoms on insulating surfaces and are commonly attributed to charge-transfer effects. For example, Au adatoms on MgO films grown on Ag (001) and on bilayer NaCl films on Cu(111) exhibit characteristic dark ring-like appearances [26,27,76,77]. Based on these comparisons, the observed ring-like features in the present study can be attributed to Fe adatoms. Au, Ag, and Cu belong to group 11 elements in the periodic table, and therefore they tend to acquire negative charges. In contrast, Fe, which belongs to group 8, is more likely to adopt a positive charge [78,79].

The height profile of the dark ring-like feature (lower-right panel in Fig. 1c) indicates a depression of approximately 20–30 pm, while the apparent height of the central Fe atom is comparable to that of the surrounding MgO surface. Interpreting this contrast is nontrivial, because the apparent height of the MgO nanoisland at V_s = +1000 mV, close to the MgO band gap, is significantly reduced under the relevant tunneling conditions, whereas the Fe atom is physically adsorbed on the MgO island with a true height of ~1 nm. Furthermore, the tunneling pathways differ between the Fe adsorption site and the bare MgO surface. At the Fe site, electrons tunnel from the STM tip through the vacuum into discrete Fe-derived states, then through the MgO insulating film to the underlying O/Fe electrode. In contrast, on the bare MgO surface, electrons tunnel directly from the STM tip through the vacuum and MgO film into the O/Fe electrode. The superposition of these distinct tunneling channels and the bias-dependent apparent-height effects likely gives rise to the observed dark ring-like contrast.

Fig. 1c illustrates the challenging nature of the imaging conditions for Fe atoms. A series of STM topographic images was acquired over the same area, in which five Fe atoms were initially observed. The region was scanned sequentially from positions labeled No 1 to No 5 while varying the applied sample bias from +1000 mV down to +850 mV and then back to +860 mV, under a constant tunneling current of 10 pA. Specifically, the sample bias was carefully tuned close to the MgO band-gap energy, thereby reducing the tunneling conductance and allowing the tip apex to approach closer to the surface. At bias voltages of +880 and +870 mV, the Fe atoms remained stable. In contrast, at +860 mV, scratch-like line features appeared near the center of the image, indicating contact between the STM tip and an Fe atom. At +850 mV, similar scratch features were observed at all atomic positions, consistent with tip contact across the surface (see also Supplementary Fig. S5). After this sequence, the same area was rescanned at +860 mV. No Fe atoms were detected, indicating that the Fe atoms had been displaced from the surface by the STM tip.

These Fe atom immobilization-mobilization is strongly related to the sample LDOS. The upper panel in Fig. 1d shows experimentally obtained dI/dV spectra plotted on a logarithmic scale, which are proportional to the surface LDOS and reveal subtle features near the gap edges. Blue and red lines correspond to the O/Fe(001) substrate and the MgO surface, respectively. The O/Fe(001) substrate exhibits no bandgap, reflecting its metallic nature, whereas the MgO insulating surface shows a clear bandgap. By comparing the MgO band structure with the STM images in Fig. 1c, we find that Fe atom immobility is directly linked to the CBM at approximately +850 mV, which coincides with the onset of atomic mobility.

The lower panel of Fig. 1d presents a diagram of STM tunneling conditions, with the x-axis representing the sample bias voltage (V_s) and the y-axis representing the tunneling current (I_t). This diagram summarizes our systematic analysis of the conditions under which Fe atoms on MgO are visible or invisible as a function of V_s and I_t. Here, we also found that the Fe atoms became readily mobile when the tunneling current setpoint was increased from 10 to 50 pA under constant-current feedback conditions (blue dots, details are shown in Fig. 2). Increasing the tunneling current forces the STM tip apex to approach closer to the sample, because the tunneling current depends exponentially on the tip–sample separation (z) : $I(z) \propto \exp(-2\kappa z)$, $\kappa = \frac{1}{\hbar}\sqrt{2m\left(\Phi - \left|\frac{eV_s}{2}\right|\right)}$, where $\hbar$ is the reduced Plank constant, m is the electron mass, Φ is the local barrier height, and e is the elementary charge [80]. In other words, increasing the tunneling current decreases the tip-sample separation z.

Fig. 1e presents schematic models illustrating the bias-dependent configurations of the STM tip apex and Fe atoms on the MgO/Fe(001) surface. In this study, Fe atoms were deposited on thick MgO nanoislands with a thickness of approximately z_{mgo} ~1.0 nm [15]. However, due to the drastic reduction in the apparent height of the MgO islands to

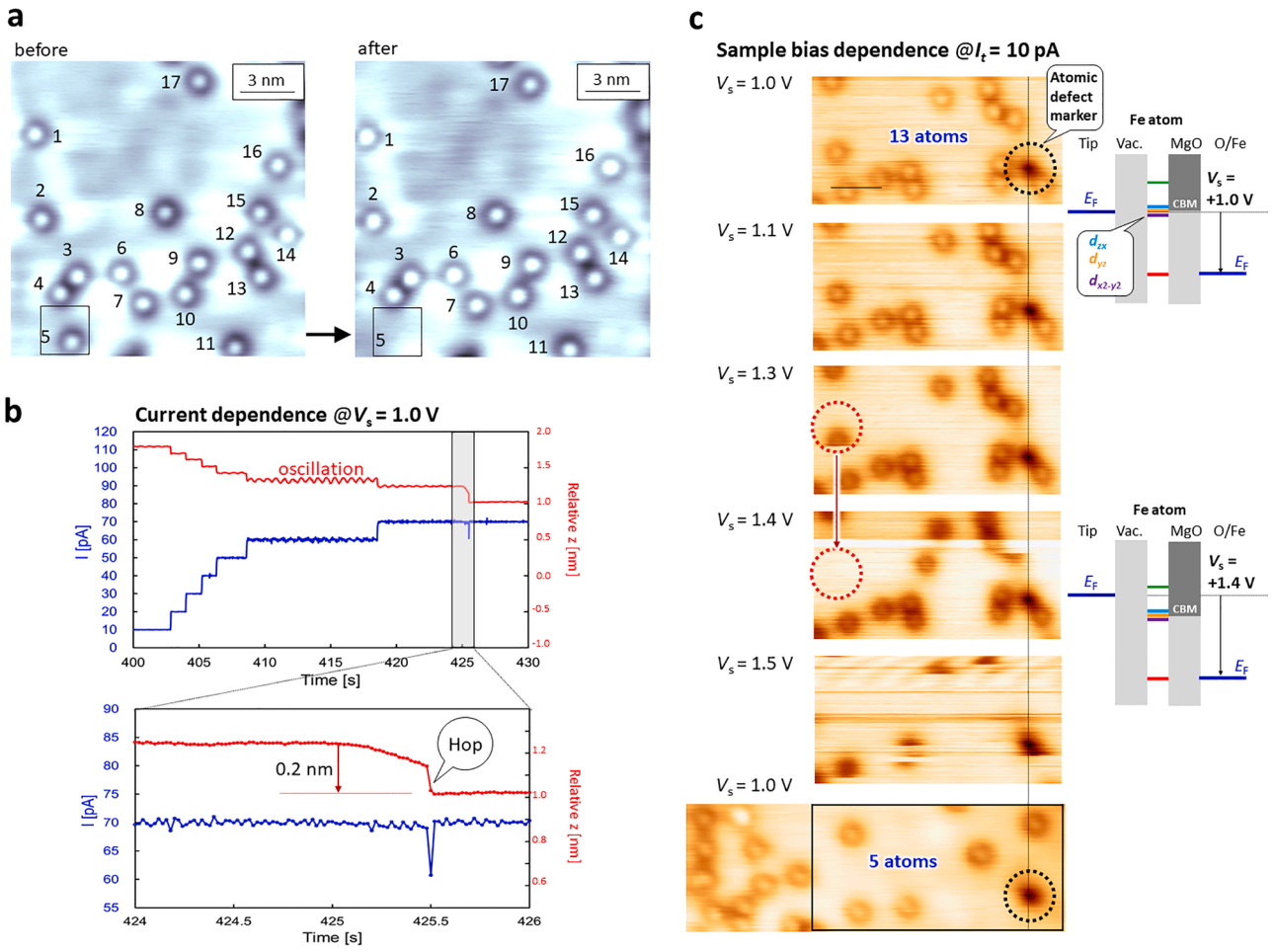

Fig. 2. STM atom displacement of Fe single atoms on MgO/Fe(001)-p(1 × 1)O. (a) STM topographic images (15 × 15 nm^2, V_s = +1.0 V, I_t = 10 pA) obtained from the same surface area of Fe single atoms adsorbed on the MgO/Fe(001)-p(1 × 1)O surface. A total of 17 Fe atoms are observed; among them, atom No 5 disappears due to STM-induced manipulation. (b) Time evolution of the tunneling current (blue) and relative tip position (red) during the hopping event of atom No 5 shown in (a). The STM tip was initially positioned above atom No 5, and the setpoint tunneling current was gradually increased in constant-current mode, bringing the tip apex closer to the atom. At t = 425 s, a sudden drop (~0.2 nm) in the relative tip height was observed, indicating that the Fe atom had hopped away from beneath the tip apex. (c) A series of STM topographic images acquired from the same area while varying the sample bias voltage from +1.0 V to +1.5 V and back to +1.0 V (I_t = 10 pA, scale bar = 3 nm). The black circle marks a defect used as a reference for identifying the same position. Red circles in the images at V_s = +1.3 V and +1.4 V indicate Fe atom manipulation induced by the STM tip proximity. Right panel: schematic energy diagrams of the double-barrier system incorporating the Fe single atom at V_s = +1.0 V (top) and +1.4 V (bottom).

~0.3 nm at V_s ~ +1000 mV (Fig. 1d), the STM tip must approach very close to the Fe atoms, as illustrated in Fig. 1e.

The tip-sample separation on the metallic O/Fe(001) surface ($z_{O/Fe}$) can be roughly estimated from the STM setpoint parameters. Although the absolute tip-sample distance cannot be measured directly, because it depends on factors such as the local work function, tip geometry, and electronic environment, it can be inferred from the tunneling resistance. Under the experimental conditions that we imaged the Fe atoms in Fig. 1c (V_s = +1 V and I_t = 10 pA), the tunneling resistance is $R = 10^{11}$ Ω. In contrast, when the tip forms a point contact with the surface, the resistance typically becomes $R = 12.9\,k\Omega$ [81]. Assuming the tip-sample distance at point contact is z_0 = 0.266 nm (the sum of the W tip apex radius, 0.140 nm, and the Fe surface atom radius, 0.126 nm), the tunneling current decays exponentially with distance as $I(z) \propto \exp(-2\kappa z)$. Taking a typical work function of the W tip (Φ_W = 4.50 eV [82]) and FeO/Fe(001) surface (Φ_{FeO} = 3.77 eV [83]), we set an effective barrier height Φ = 4.135 eV. With this value, a 0.1 nm increase in tip-sample distance increases the resistance by a factor of approximately 8. Using this exponential relation, a resistance of R = 10 [11]. Ω corresponds to a tip-sample separation on the O/Fe(001) metallic surface of $z_{O\backslash Fe} \approx z_0 + \frac{\ln(R/R_0)}{2\kappa} \approx 0.266 + 0.812 = 1.078$ nm. Then, we experimentally determined the apparent height (z_A) of the MgO terraces as a function of the sample bias voltage. Red dots in Fig. 1e indicate the experimentally measured z_A. Within the MgO bandgap, the apparent height is nearly zero, whereas z_A increases starting from the CBM and rises almost linearly with increasing bias, reaching a maximum at V_s = +4 V. Finally, we can estimate the distance between the STM tip and the Fe atom at V_s = +1 V and I_t = 10 pA as: $z = z_{O/Fe} + z_A - z_{mgo} - z_{Fe} \sim 0.13$ nm, where z_{Fe} = 0.252 nm is the Fe atom diameter. This extremely short tip-sample distance highlights the delicate nature of the tunneling configuration required to visualize individual Fe atoms on the MgO surface. Therefore, a slight reduction of the sample bias toward the MgO band gap, from +1000 mV to +850 mV in Fig. 1c, drives the STM tip apex even closer to the Fe atom, ultimately leading to tip–atom contact at +850 mV and resulting in the displacement of the Fe atom on the MgO surface.

To further clarify this, we compared the experimentally observed region to the energy positions of the Fe discrete orbitals relative to the Fermi energy (E_F). The grey peaks in Fig. 1d shows the DFT-calculated total LDOS, indicating the positions of the discrete Fe 3d orbitals. Because STM measures the tunneling current, which for positive sample bias is dominated by the integrated LDOS above the Fermi energy (E - E_F

= 0 eV), the absence of Fe-derived orbitals up to approximately +850 meV, corresponding to the MgO CBM, plays a crucial role. In this energy range, the tunneling current is not mediated by Fe atomic states, forcing the STM tip to approach closer to the surface to maintain a constant current. The combination of this enhanced tip approach and the lack of Fe orbital contributions below +850 meV explains why Fe atoms are displaced by the scanning tip.

These experimentally identified conditions could suggest STS measurements to be performed by setting the bias and current setpoints to $V_s \sim 1$ V and $I_t \leq 50$ pA, respectively. These parameters fix the tip–sample separation (z) while maintaining the immobilization of the Fe atom, thereby allowing the detection of quantum spin signals such as a zero-bias peak (ZBP) within the energy gap, similar to the case of CuPc molecules on MgO surfaces [16].

3.2. Fe adatom displacement on insulating surface

As shown in Fig. 1, the range of stable conditions for atoms in such double-barrier systems is extremely limited. To further investigate Fe atoms adsorbed on MgO insulating surfaces, we systematically studied the conditions under which individual atoms can be displaced by gently approaching the STM tip apex [32,84].

Fig. 2a shows isolated Fe atoms, numbered 1–17. The STM image in the left panel of Fig. 2a was acquired with a setpoint bias of 1 V and a tunneling current of 10 pA. We then positioned the tip apex directly above atom No 5 (marked by the black box) and gradually increased the tunneling current in constant-current mode with feedback, while simultaneously monitoring the tip position. The resulting variations over time are shown in Fig. 2b. From $I_t = 10$ pA to 50 pA (blue line), the tip apex moved closer to atom No 5 (red line) by 0.27 nm, with steps determined by the feedback loop. At $I_t = 60$ pA, oscillatory variations appeared, which may indicate pulling and pushing interactions between the W tip apex and the Fe atom. When the current was further increased to 70 pA, the Fe atom hopped beneath the tip, causing a sudden drop in the tunneling current. The feedback loop subsequently adjusted the tip position to maintain the setpoint tunneling current at $t = 425.5$ s. Because the hopping process is much faster than the feedback loop's response time, the current trace, recorded every 20 ms, shows a sharp dip (lower panel of Fig. 2b). Interestingly, just before the final hopping event, the tunneling current was slightly below the setpoint (~1 pA), causing a minor tip shift between $t = 425$ s and $t = 425.5$ s. This can be explained by repeated hopping of the Fe atom in and out of the junction at frequencies higher than the experimental time resolution. The right panel of Fig. 2a shows the same area after the hopping event; only Fe atom No 5 has disappeared.

We still face an open question as to why Fe atoms are also displaced at bias voltages much higher than the CBM, as shown in Fig. 1b The origin of this atomic displacement must be different from the mechanism depicted in Fig. 1c, where the bias is tuned close to the MgO band gap. Thus, we also investigated the effect of bias voltage on Fe atom manipulation. Fig. 2c presents a series of STM topographic images at a fixed tunneling current of 10 pA. The same 15×8 nm^2 area was scanned repeatedly while gradually increasing the bias from +1.0 V to +1.5 V and then returning to +1.0 V. A black circle marks a defect on the MgO surface used as a reference to track the same locations. At +1.0 V, 13 atoms were observed; however, the atom marked by the red circle disappeared between +1.3 V and +1.4 V, and by +1.5 V, most atoms were disturbed. Rescanning the same area at +1.0 V revealed only 5 remaining atoms, while the positions of these 5 atoms differed from their original locations. Although the mechanism underlying Fe atom displacement at higher bias voltages remains unclear, one possible trigger is the strong electric field, particularly given that an electric field of approximately 5.5 GV/m has been reported to induce the bcc–fcc phase transition in Fe, *i.e.*, the magnetoelectric coupling observed in Fe bilayer films on Cu(111) [48,49,85]. In general, increasing the sample bias enhances the electric field E(in GV/m). At the same time, the STM tip apex retracts from the surface because the apparent height of the MgO layer increases with increasing bias (Fig. 1e). As a result, even slight variations in the electric field may determine whether Fe atoms on MgO/Fe(001) remain immobile or become displaced. We could estimate the electric field E (in GV/m) acting on the Fe atom within the double-barrier system as follows. A sample bias voltage (V_s) is applied between the STM tip and the Fe(001) substrate, with the voltage drop distributed across two regions: the vacuum gap (V_{vac}) and the MgO layer (V_{mgo}) [86,87]. The vacuum voltage drop can be expressed as $V_{vac} = V_{mgo}(\varepsilon_{mgo} / \varepsilon_{vac})(z / z_{mgo})$ and $V_s = V_{vac} + V_{mgo}$, where ε_{mgo} and ε_{vac} are the dielectric constants of the MgO nanoislands and vacuum, respectively. Considering that the dielectric constant decreases from 9.8 in bulk MgO to 8.2 in nanoislands [88], we used $\varepsilon_{mgo} / \varepsilon_{vac} = 8.2$. The electric field at the Fe atom can then be calculated as $E = V_{vac} / z$. Therefore, most of the electric field is expected to drop across the vacuum region rather than the MgO layers. Under these conditions, the Fe atom on MgO/Fe(001) at a sample bias of $V_s = +1$ V is estimated to experience an electric field of approximately 3 GV/m. In other words, although we are able to observe Fe atoms on MgO/Fe(001), these atoms are subjected to a very high electric field. Therefore, it is reasonable that even a slight increase in the electric field can readily displace the atoms.

Thus, we conclude that Fe atoms on MgO/Fe(001) can be stabilized within an applied bias range from +860 mV to +1300 mV, that is, just above the conduction-band minimum of MgO.

3.3. DFT insights of Fe atom charging

Finally, we discuss the charging of the Fe atom adsorbed on MgO/O/Fe(001) using DFT results. Fig. 3a shows the partial DOS for the adsorbed Fe atom (blue line), the oxygen atom directly below the Fe atom (O1, red line), and its neighboring oxygen atom (O2, orange line). The results reveal orbital hybridization between the Fe and O1 atoms.

The eigenvalues of singly occupied orbitals of an isolated Fe atom are significantly positive, and the Fe has a low work function. Therefore, electron transfer from Fe is expected. Since MgO is an insulator, the transferred electron from Fe would be accommodated in the MgO valence band (*i.e.*, the Mg-*s*–derived band). However, the electron transfer is difficult due to the large band gap of MgO. We calculated the adsorption of Fe atoms onto Mg, which can interact most strongly with Mg, but this adsorption is significantly less stable than Fe adsorption onto O (Fig. S7 in Supporting Information). In addition, the previous study where Fe adsorption on MgO/Ag(001) is investigated also adopted the on-top of O as the stable site, and no significant electron transfer from Fe to the valence bands was confirmed[29,78,79]. The O interacting with Fe possess fully filled 2*p* orbitals in its valence shell, leaving no capacity to accept excess electrons. Orbital correlations between O 2*p* and Fe 3*d* orbitals are confirmed from the PDOS. The orbitals in $-5 < E - E_F < -6$ eV has a large O character, while those in $-3 < E - E_F < +2$ eV has a large Fe character (Fig. 3a). Note that, the hybridized orbitals downshift according to high electronegativity of O. Hence, although the character of the Fe atom remains, its electron distribution is strongly pulled towards the O side. Taking into account the large polarization in Fe–O hybridization, this study assumes that the formal charge of adsorbed Fe is not zero. This electronic state is consistent with previously reported DFT calculations for the MgO/Ag system [29,79]; therefore, we conclude that substrate effects can be neglected (*i.e.*, MgO effectively acts as a screening layer).

The spin mapping of the Fe atom on MgO/O/Fe(001), shown from the top view in Fig. 3b and the side view in Fig. 3c, indicates that the Fe atom is spin-polarized. This is consistent with the case of Fe atoms adsorbed on MgO/Ag(001) [29], as the electronic influence of the Fe (001) substrate is confined to below the first MgO layer. Therefore, the surface Fe atom shows no significant differences between the Fe and Ag substrates.

The difference in electron distribution before and after the adsorption of the Fe atom, shown in Fig. 3d, reveals that the reduction in

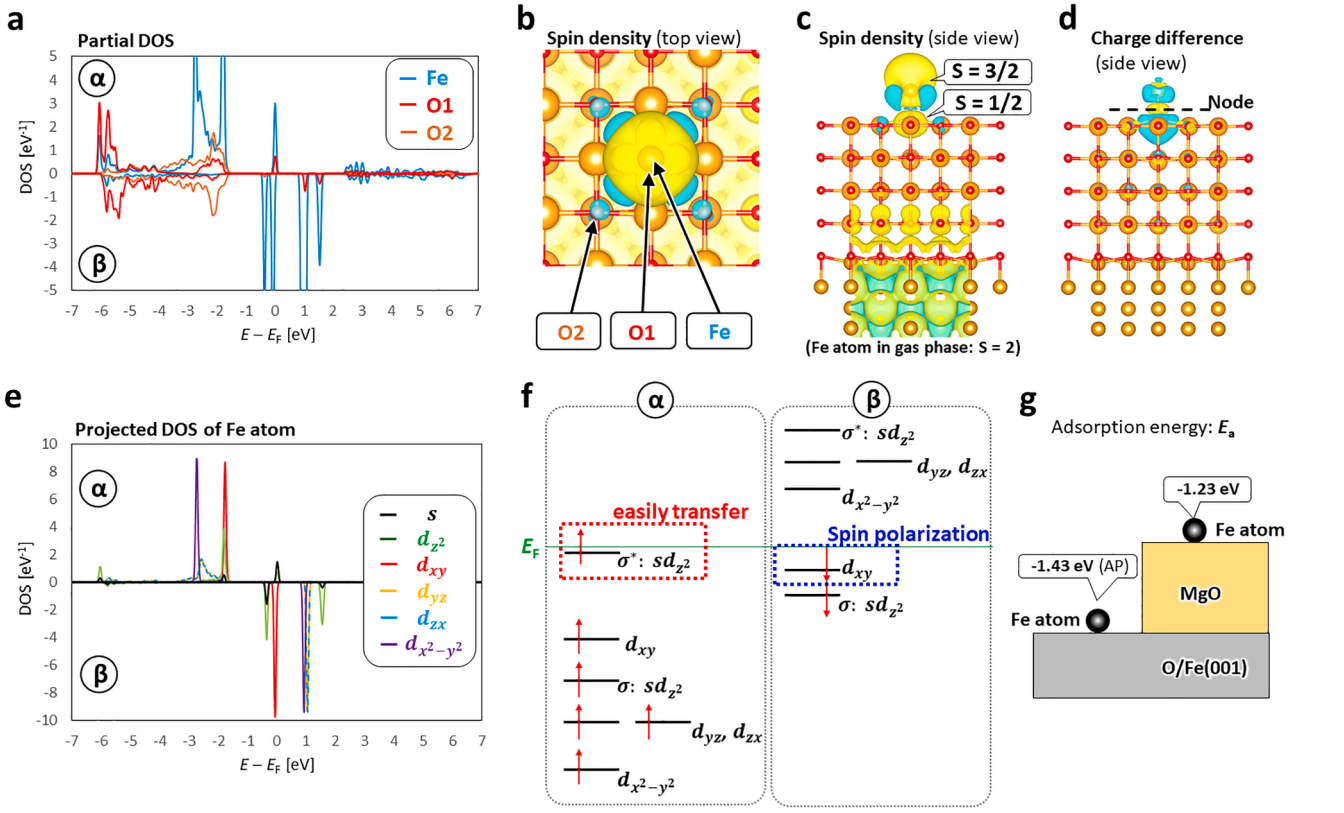

Fig. 3. DFT analysis of positively charged Fe atom on s on MgO/Fe(001)-p(1 × 1)O. (a) Partial DOS of Fe and adsorbing O atoms, (b) top view of spin density distribution, (c) side view of spin density distribution, (d) charge difference distribution before and after the Fe atom adsorption. Yellow and blue distribution for charge difference represent the increase and decrease of electrons, respectively. (e) Projected DOS of adsorbed Fe atom, (f) schematic view of *d* orbital split with O-coordination field. E_F denotes the Fermi energy. Yellow and blue distribution for spin density represent major and minor spins, respectively. The threshold for spin density and electron difference distributions are 0.0005 and 0.0015 a.u., respectively. (g) Spherical models of Fe atoms on O/Fe(001) and MgO surfaces, with adsorption energies of −1.43 eV for the antiparallel (AP) configuration, and −1.23 eV for the MgO surface, respectively.

electron density is due to the antibonding interaction between the Fe atom and the oxygen atom directly below it. A node is observed in the electron-depleted region (yellow area). From the charge maps in Figs. 3b-d, the atomic charge of the adsorbed Fe atom on the MgO surface can be estimated using the Bader charge analysis. The number of valence electrons in the free-standing Fe atom, which is 8.000, decreases to 6.930 for the adsorbed Fe atom, resulting in an atomic charge of $q = +1.070$. This indicates that the charge-polarization between adsorbed Fe atom and O^{2-} in MgO is so large that spin momentum of Fe is approximately 3/2.

To gain a deeper understanding of the Fe atom adsorbed on the MgO surface, the projected DOS is shown in Fig. 3e, where the five degenerate 3*d* orbitals split into four distinct 3*d* orbitals. This splitting is not explained via the crystal field induced by oxygen ions (Supplementary, Fig. S2), and the ligand fields surrounding the Fe atom on the MgO surface are required (Fig. 3f), *i.e.*, the orbital overlap between Fe and O atoms is important for understanding the electronic state of Fe adatom. In the gas phase, the unoccupied *s* and d_{z2} orbitals can form coordination bonds with oxygen atoms. The d_{z2} and *s* orbital peaks, located near the Fermi energy, indicate electronic hybridization between these orbitals, as they are positioned at the same energy level, resulting in an *s*-d_{z2} hybridized σ orbital with O p_z orbital (Fig. 3f). The projected DOS for oxygen ion adsorbing Fe is shown in Supplementary Fig. S3. This σ bonding orbital is stable, while the antibonding σ* orbital is unstable. Consequently, the σ* orbital could interact with the oxygen ion (lone pair), forming a p_z-sd_{z2} bonding interaction between the Fe and O1 atoms. This bonding plays a significant role in the adsorption of the Fe atom on the insulating MgO surface. Other Fe orbitals, such as d_{yz}, d_{zx}, and d_{x2-y2}, can interact with oxygen but d_{xy} cannot interact. These interactions split the degeneracy between d_{xy} and d_{x2-y2}, while the degeneracy of d_{yz} and d_{zx} is maintained, producing four split bands. Additionally, all α-orbitals are occupied, and the electron-electron Coulomb repulsion between α and β-orbitals causes the β-orbitals to shift upwards, enhancing the instability.

Upon closer inspection of the antibonding σ* orbitals, we find these exist in both α and β states. The σ* orbital in the α-states is relatively more stable near the Fermi energy. In contrast, the σ* orbital in the β-states resides at much higher energy levels in the unoccupied states, making it more unstable. We plot all the Fe *d*-orbitals of the Fe atom adsorbed on the MgO surface in Fig. 3f, and gradually fill the electron spins (indicated by red arrows) from the lowest energy level (full energy diagram including O *p*-orbitals is shown in Supplementary Fig. S3). The highest occupied orbital is found to be the antibonding σ* orbital in the α-states. Antibonding orbitals typically prefer not to be occupied by electron spins, and the occupation of the σ* orbital destabilizes the Fe-O bonding. This instability is likely the primary cause of the charging of the Fe atom on the MgO surface. Since the σ* orbital is located near the Fermi energy, the electrons in this orbital can escape, resulting in a charged Fe atom. This partial electron removal from the σ* orbital, crossing the Fermi energy, produces the peak in the LDOS near the Fermi energy (Fig. 3e).

This suggests that, during the antibonding formation of the σ* orbital, electronic hybridization occurs between the sd_{z2} and p_z orbitals, with one electron pulling from the Fe d_{z2} orbital to the oxygen p_z orbital. In the orbital diagrams of Fig. 3f, all *d*- and *s*-orbitals in the α-state are occupied by electron spins. Consequently, the majority spin distribution adopts a roughly spherical shape, but inaccuracies in bonding with oxygen elongate this sphere along the *z*-direction. In the β-state, the d_{xy}

orbital, which has the lowest electrostatic repulsion with the O *p*-orbitals, and the very stable d_{z2} orbital due to the orbital overlap are occupied. Other orbitals in the β-states, which elongate along the *z*-direction, are not occupied due to instability induced by the ligand fields. Since the occupied d_{xy} orbital extends into the *x*-*y* plane, the spin-polarized DOS is distributed around the Fe atom.

Finally, from the DFT results shown in Fig. 3, we obtained an adsorption energy of $E_a = -1.23$ eV for a single Fe atom on the MgO/Fe (001) surface. This adsorption is weaker than that of Fe atoms on the O/Fe(001) metallic surface, which has adsorption energies of –1.43 eV. Nevertheless, it is comparable to typical one-electron chemical bonding, as summarized in Fig. 3g. This negative adsorption energy indicates that Fe atoms on MgO/Fe(001) are energetically stable.

4. Conclusions

We investigated the robustness of Fe atom adsorption on the widely used spintronic system MgO/Fe(001) with an MgO thickness of approximately 1 nm, using atomically resolved STM. This double-barrier configuration effectively decouples the Fe atom's spin from conduction electrons, protecting it from spin screening, inelastic spin-flip scattering, and spin relaxation.

Although we find that a thick insulating film with a thickness comparable to the STM tip–sample separation makes imaging adatoms near the Fermi energy within the band gap extremely challenging, this difficulty arises from the STM tip approaching the surface very closely, often reaching near-contact conditions that induce adatom mobility. Despite this limitation, we experimentally identify a critical tunneling condition just above the MgO CBM, under which Fe atoms can be stabilized on the thick MgO surface by employing low tunneling currents below 50 pA.

Although STM imaging under these conditions remains challenging, the Fe adatoms are robustly adsorbed on the MgO surface through orbital hybridization and charge transfer. As revealed by DFT calculations, neutral Fe atoms are converted into a cationic state with an effective spin of $S \approx 3/2$, as crystal- and ligand-field effects lift the degeneracy of the Fe 3*d* orbitals and give rise to discrete electronic states that host stable quantum spins.

These findings establish Fe atoms on the MgO/Fe(001) system as robust, chemically bonded, and electronically decoupled spin centers, offering a promising platform for atomic-scale quantum spin devices.

CRediT authorship contribution statement

Toyo Kazu Yamada: Writing – review & editing, Writing – original draft, Visualization, Validation, Supervision, Resources, Project administration, Methodology, Investigation, Funding acquisition, Formal analysis, Data curation, Conceptualization. **Nana K.M. Nazriq:** Investigation, Formal analysis, Data curation. **Kohei Tada:** Writing – review & editing, Supervision, Software, Formal analysis.

Declaration of competing interest

There are no conflicts to declare.

Acknowledgments

This work was supported by JSPS KAKENHI Grant Number 17K19023, 22H02050, 23K23318, and 23H02033, the Murata Science Foundation, the Shorai Foundation for Science and Technology, the TEPCO Memorial Foundation, the Casio Science Promotion Foundation, and the Toshiaki Ogasawara Memorial Foundation. The computations in this study were performed using facilities at the Supercomputer Centre, Institute for Solid State Physics, University of Tokyo. We thank Dr. Lukas Gerhard for the fruitful discussion of applying the electric field from the STM tip.

Supplementary materials

Supplementary material associated with this article can be found, in the online version, at doi:10.1016/j.apsadv.2026.100965.

Data availability

Data will be made available on request.

References

[1] T.M. Graham, Y. Song, J. Scott, C. Poole, L. Phuttitarn, K. Jooya, P. Eichler, X. Jiang, A. Marra, B. Grinkemeyer, M. Kwon, M. Ebert, J. Cherek, M.T. Lichtman, M. Gillette, J. Gilbert, D. Bowman, T. Ballance, C. Campbell, E.D. Dahl, O. Crawford, N.S. Blunt, B. Rogers, T. Noel, M. Saffman, Multi-qubit entanglement and algorithms on a neutral-atom quantum computer, Nature 604 (7906) (2022) 457–462, https://doi.org/10.1038/s41586-022-04603-6.

[2] J.J. Pla, K.Y. Tan, J.P. Dehollain, W.H. Lim, J.J.L. Morton, D.N. Jamieson, A. S. Dzurak, A. Morello, A single-atom electron spin Qubit in silicon, Nature 489 (7417) (2012) 541–545, https://doi.org/10.1038/nature11449.

[3] T.M. Graham, M. Kwon, B. Grinkemeyer, Z. Marra, X. Jiang, M.T. Lichtman, Y. Sun, M. Ebert, M. Saffman, Rydberg-mediated entanglement in a two-dimensional neutral atom qubit array, Phys. Rev. Lett. 123 (23) (2019) 230501, https://doi.org/10.1103/PhysRevLett.123.230501.

[4] Y. Wang, Y. Chen, H.T. Bui, C. Wolf, M. Haze, C. Mier, J. Kim, D.-J. Choi, C.P. Lutz, Y. Bae, S. Phark, A.J. Heinrich, An atomic-scale multi-qubit platform, Science 382 (6666) (2023) 87–92, https://doi.org/10.1126/science.ade5050.

[5] A.J. Heinrich, J.A. Gupta, C.P. Lutz, D.M. Eigler, Single-atom spin-flip spectroscopy, Science 306 (5695) (2004) 466–469, https://doi.org/10.1126/science.1101077.

[6] D.-J. Choi, N. Lorente, J. Wiebe, K. Von Bergmann, A.F. Otte, A.J. Heinrich, Colloquium : atomic spin chains on surfaces, Rev. Mod. Phys. 91 (4) (2019) 041001, https://doi.org/10.1103/RevModPhys.91.041001.

[7] S. Reale, A. Singha, S.L. Ahmed, D. Krylov, L. Colazzo, C. Wolf, C.S. Casari, A. Barla, E. Fernandes, F. Patthey, M. Pivetta, S. Rusponi, H. Brune, F. Donati, Erbium and thulium on MgO(100)/Ag(100) as candidates for single atom qubits, Phys. Rev. B 107 (4) (2023) 045427, https://doi.org/10.1103/PhysRevB.107.045427.

[8] V. Madhavan, W. Chen, T. Jamneala, M.F. Crommie, N.S. Wingreen, Tunneling into a single magnetic atom: spectroscopic evidence of the Kondo resonance, Science 280 (5363) (1998) 567–569, https://doi.org/10.1126/science.280.5363.567.

[9] O.Yu. Kolesnychenko, R. De Kort, M.I. Katsnelson, A.I. Lichtenstein, H. Van Kempen, Real-space imaging of an orbital kondo resonance on the Cr(001) surface, Nature 415 (6871) (2002) 507–509, https://doi.org/10.1038/415507a.

[10] O. Újsághy, J. Kroha, L. Szunyogh, A. Zawadowski, Theory of the fano resonance in the STM tunneling density of states due to a single Kondo impurity, Phys. Rev. Lett. 85 (12) (2000) 2557–2560, https://doi.org/10.1103/PhysRevLett.85.2557.

[11] A. Mugarza, C. Krull, R. Robles, S. Stepanow, G. Ceballos, P. Gambardella, Spin coupling and relaxation inside molecule–Metal contacts, Nat. Commun. 2 (1) (2011) 490, https://doi.org/10.1038/ncomms1497.

[12] J. Fransson, Spin inelastic electron tunneling spectroscopy on local Spin adsorbed on surface, Nano Lett. 9 (6) (2009) 2414–2417, https://doi.org/10.1021/nl901066a.

[13] M. Moors, A. Krupski, S. Degen, M. Kralj, C. Becker, K. Wandelt, Scanning tunneling microscopy and spectroscopy investigations of copper phthalocyanine adsorbed on Al2O3/Ni3Al(111), Appl. Surf. Sci. 254 (14) (2008) 4251–4257, https://doi.org/10.1016/j.apsusc.2008.01.029.

[14] F. Donati, S. Rusponi, S. Stepanow, C. Wäckerlin, A. Singha, L. Persichetti, R. Baltic, K. Diller, F. Patthey, E. Fernandes, J. Dreiser, Ž. Šljivančanin, K. Kummer, C. Nistor, P. Gambardella, H. Brune, Magnetic remanence in single atoms, Science 352 (6283) (2016) 318–321, https://doi.org/10.1126/science.aad9898.

[15] K.M. Nazriq, N. Krüger, P. Kazu Yamada, T improving MgO/Fe insulator-metal interface structure through oxygen-precoating of Fe(0 0 1), Appl. Surf. Sci. 618 (2023) 156628, https://doi.org/10.1016/j.apsusc.2023.156628.

[16] K. Ishii, N.K.M. Nazriq, P. Krüger, T.K. Yamada, Emergence of a zero-bias peak on the MgO/Fe(001) surface induced by the adsorption of a spin-1/2 molecule, Nanoscale Horiz 10 (10) (2025) 2454–2464, https://doi.org/10.1039/D5NH00192G.

[17] T.C. Hung, B. Kiraly, J.H. Strik, A.A. Khajetoorians, D. Wegner, Plasmon-driven motion of an individual molecule, Nano Lett 21 (12) (2021) 5006–5012, https://doi.org/10.1021/acs.nanolett.1c00788.

[18] K.A. Cochrane, T.S. Roussy, B. Yuan, G. Tom, E. Mårsell, S.A Burke, Molecularly resolved electronic landscapes of differing acceptor–Donor interface geometries, J. Phys. Chem. C 122 (15) (2018) 8437–8444, https://doi.org/10.1021/acs.jpcc.8b01396.

[19] C.F. Hirjibehedin, C.P. Lutz, A.J. Heinrich, Spin coupling in engineered atomic structures, Science 312 (5776) (2006) 1021–1024, https://doi.org/10.1126/science.1125398.

[20] S. Ohno, K. Nakatsuji, F. Komori, Initial growth of Fe nano-islands on Cu(001)-c (2×2)N surfaces, JPN. J. Appl. Phys. 42 (2003) 4701–4705, https://doi.org/10.1143/JJAP.42.4701. Part 1, No. 7B.

[21] R. Kawaguchi, K. Hashimoto, T. Kakudate, K. Katoh, M. Yamashita, T. Komeda, Spatially resolving electron spin resonance of π-radical in single-molecule magnet, Nano Lett 23 (1) (2023) 213–219, https://doi.org/10.1021/acs.nanolett.2c04049.
[22] X. Zhang, C. Wolf, Y. Wang, H. Aubin, T. Bilgeri, P. Willke, A.J. Heinrich, T. Choi, Electron spin resonance of single iron phthalocyanine molecules and role of their non-localized spins in magnetic interactions, Nat. Chem. 14 (1) (2022) 59–65, https://doi.org/10.1038/s41557-021-00827-7.
[23] L. Sellies, R. Spachtholz, S. Bleher, J. Eckrich, P. Scheuerer, J. Repp, Single-molecule electron spin resonance by means of atomic force microscopy, Nature 624 (7990) (2023) 64–68, https://doi.org/10.1038/s41586-023-06754-6.
[24] F. Nishino, P. Krüger, C. Wang, R. Nemoto, Y. Chang, T. Hosokai, Y. Hasegawa, K. Fukutani, S. Kera, M. Horie, T.K. Yamada, Reversible sliding motion by hole-injection in ammonium-linked ferrocene, electronically decoupled from noble metal substrate by crown-ether template layer, Small 21 (17) (2025) 2408217, https://doi.org/10.1002/smll.202408217.
[25] I. Swart, T. Sonnleitner, J. Niedenführ, J. Repp, Controlled lateral manipulation of molecules on insulating films by STM, Nano Lett 12 (2) (2012) 1070–1074, https://doi.org/10.1021/nl204322r.
[26] M. Sterrer, T. Risse, U. Martinez Pozzoni, L. Giordano, M. Heyde, H.P. Rust, G. Pacchioni, H.J. Freund, Control of the charge State of metal atoms on thin MgO films, Phys. Rev. Lett. 98 (9) (2007) 096107, https://doi.org/10.1103/PhysRevLett.98.096107.
[27] G. Pacchioni, L. Giordano, M. Baistrocchi, Charging of metal atoms on ultrathin MgO /Mo (100) films, Phys. Rev. Lett. 94 (22) (2005) 226104, https://doi.org/10.1103/PhysRevLett.94.226104.
[28] E. Fernandes, F. Donati, F. Patthey, S. Stavrić, Ž. Šljivančanin, H. Brune, Adsorption sites of individual metal atoms on ultrathin MgO(100) films, Phys. Rev. B 96 (4) (2017) 045419, https://doi.org/10.1103/PhysRevB.96.045419.
[29] S. Baumann, F. Donati, S. Stepanow, S. Rusponi, W. Paul, S. Gangopadhyay, I. G. Rau, G.E. Pacchioni, L. Gragnaniello, M. Pivetta, J. Dreiser, C. Piamonteze, C. P. Lutz, R.M. Macfarlane, B.A. Jones, P. Gambardella, A.J. Heinrich, H. Brune, Origin of perpendicular magnetic anisotropy and large orbital moment in Fe atoms on MgO, Phys. Rev. Lett. 115 (23) (2015) 237202, https://doi.org/10.1103/PhysRevLett.115.237202.
[30] Baumann, S., Donati, F., Stepanow, S., Rusponi, S., Paul, W., Gangopadhyay, S., Rau, I.G., Pacchioni, G.E., Gragnaniello, L., Pivetta, M., Dreiser, J., Piamonteze, C., Lutz, C.P., Macfarlane, R.M., Jones, B.A., Gambardella, P., Heinrich, A.J., Brune, H. Interplay between orbital magnetic moment and crystal field symmetry: fe atoms on MgO. arXiv 2015. https://doi.org/10.48550/ARXIV.1506.07807.
[31] A. Singha, F. Donati, F.D. Natterer, C. Wäckerlin, S. Stavrić, Z.S. Popović, Ž. Šljivančanin, F. Patthey, H. Brune, Spin excitations in a 4 f − 3 d heterodimer on MgO, Phys. Rev. Lett. 121 (25) (2018) 257202, https://doi.org/10.1103/PhysRevLett.121.257202.
[32] L. Bartels, G. Meyer, K.-H. Rieder, Basic steps of lateral manipulation of single atoms and diatomic clusters with a scanning tunneling microscope tip, Phys. Rev. Lett. 79 (4) (1997) 697–700, https://doi.org/10.1103/PhysRevLett.79.697.
[33] M.F. Crommie, C.P. Lutz, D.M. Eigler, Confinement of electrons to quantum corrals on a metal surface, Science 262 (5131) (1993) 218–220, https://doi.org/10.1126/science.262.5131.218.
[34] S. Kawai, A.S. Foster, F.F. Canova, H. Onodera, S. Kitamura, E. Meyer, Atom manipulation on an insulating surface at room temperature, Nat. Commun. 5 (1) (2014) 4403, https://doi.org/10.1038/ncomms5403.
[35] A. Mena, S.K. Mann, A. Cowley-Semple, E. Bryan, S. Heutz, D.R. McCamey, M. Attwood, S.L. Bayliss, Room-temperature optically detected coherent control of molecular spins, Phys. Rev. Lett. 133 (12) (2024) 120801, https://doi.org/10.1103/PhysRevLett.133.120801.
[36] Z. Li, K. Schouteden, V. Iancu, E. Janssens, P. Lievens, C. Van Haesendonck, J. I. Cerdá, Chemically modified STM tips for atomic-resolution imaging of ultrathin NaCl films, Nano Res 8 (7) (2015) 2223–2230, https://doi.org/10.1007/s12274-015-0733-y.
[37] F.E. Olsson, S. Paavilainen, M. Persson, J. Repp, G. Meyer, Multiple charge states of Ag atoms on ultrathin NaCl films, Phys. Rev. Lett. 98 (17) (2007) 176803, https://doi.org/10.1103/PhysRevLett.98.176803.
[38] W. Huang, K.H. Au-Yeung, P. Greule, M. Stark, C. Sürgers, W. Wernsdorfer, R. Robles, N. Lorente, P. Willke, An electrically controlled single-molecule spin switch, Nat. Commun. 16 (1) (2025) 8242, https://doi.org/10.1038/s41467-025-63574-0.
[39] S.S.P. Parkin, C. Kaiser, A. Panchula, P.M. Rice, B. Hughes, M. Samant, S.-H. Yang, Giant tunnelling magnetoresistance at room temperature with MgO (100) tunnel barriers, Nat. Mater. 3 (12) (2004) 862–867, https://doi.org/10.1038/nmat1256.
[40] S. Yuasa, T. Nagahama, A. Fukushima, Y. Suzuki, K. Ando, Giant room-temperature magnetoresistance in single-crystal Fe/MgO/Fe magnetic tunnel junctions, Nat. Mater. 3 (12) (2004) 868–871, https://doi.org/10.1038/nmat1257.
[41] Scheike, T., Wen, Z., Sukegawa, H., Mitani, S. Giant oscillatory tunnel magnetoresistance in CoFe/MgO/CoFe(001) junctions. arXiv 2022. https://doi.org/10.48550/ARXIV.2202.07847.
[42] R. Matsumoto, A. Fukushima, T. Nagahama, Y. Suzuki, K. Ando, S. Yuasa, Oscillation of giant tunneling magnetoresistance with respect to tunneling barrier thickness in fully epitaxial Fe/MgO/Fe magnetic tunnel junctions, Appl. Phys. Lett. 90 (25) (2007) 252506, https://doi.org/10.1063/1.2750398.
[43] N.K.M. Nazriq, P. Krüger, T.K. Yamada, Carbon monoxide stripe motion driven by correlated lateral hopping in a 1.4 × 1.4 monolayer phase on Cu(111), J. Phys. Chem. Lett. 11 (5) (2020) 1753–1761, https://doi.org/10.1021/acs.jpclett.9b03645.
[44] I. Horcas, R. Fernández, J.M. Gómez-Rodríguez, J. Colchero, J. Gómez-Herrero, A. M. Baro, WSXM: a software for scanning probe microscopy and a tool for nanotechnology, Rev. Sci. Instrum. 78 (1) (2007) 013705, https://doi.org/10.1063/1.2432410.
[45] T.K. Yamada, T. Abe, N.M.K. Nazriq, T. Irisawa, Electron-bombarded ⟨110⟩-oriented tungsten tips for stable tunneling Electron emission, Rev. Sci. Instrum. 87 (3) (2016) 033703, https://doi.org/10.1063/1.4943074.
[46] T. Yamaguchi, E. Inami, Y. Goto, Y. Sakai, S. Sasaki, T. Ohno, T.K. Yamada, Fabrication of tungsten tip probes within 3 s by using flame etching, Rev. Sci. Instrum. 90 (6) (2019) 063701, https://doi.org/10.1063/1.5085251.
[47] Y. Goto, R. Suizu, Y. Noguchi, T.K. Yamada, Oxidative vaporization etching for molybdenum tip formation in air, Appl. Surf. Sci. 542 (2021) 148642, https://doi.org/10.1016/j.apsusc.2020.148642.
[48] T.K. Yamada, L. Gerhard, T. Balashov, A.F. Takács, R.J.H. Wesselink, W. Wulfhekel, Electric field control of Fe nano magnets: towards metallic nonvolatile data storage devices, Jpn. J. Appl. Phys. 50 (8) (2011), https://doi.org/10.1143/JJAP.50.08LA03, 08LA03.
[49] L. Gerhard, T.K. Yamada, T. Balashov, A.F. Takács, R.J.H. Wesselink, M. Däne, M. Fechner, S. Ostanin, A. Ernst, I. Mertig, W. Wulfhekel, Magnetoelectric coupling at metal surfaces, Nat. Nanotechnol. 5 (11) (2010) 792–797, https://doi.org/10.1038/nnano.2010.214.
[50] T.K. Yamada, Y. Yamagishi, S. Nakashima, Y. Kitaoka, K. Nakamura, Role of π − d hybridization in a 300-K organic-magnetic interface: metal-free phthalocyanine single molecules on a bcc Fe(001) whisker, Phys. Rev. B 94 (19) (2016) 195437, https://doi.org/10.1103/PhysRevB.94.195437.
[51] T.K. Yamada, H. Tamura, M. Shishido, T. Irisawa, T. Mizoguchi, Surface reconstruction of clean bcc-Fe{110}: a quasi-hexagonal top-layer with periodic height modulation, Surf. Sci. 603 (2) (2009) 315–319, https://doi.org/10.1016/j.susc.2008.11.010.
[52] T.K. Yamada, M.M.J. Bischoff, G.M.M. Heijnen, T. Mizoguchi, H. van Kempen, Observation of spin-polarized surface states on ultrathin bct Mn(001) films by spin-polarized scanning tunneling spectroscopy, Phys. Rev. Lett. 90 (5) (2003) 056803, https://doi.org/10.1103/PhysRevLett.90.056803.
[53] A. Bagrets, S. Schmaus, A. Jaafar, D. Kramczynski, T.K. Yamada, M. Alouani, W. Wulfhekel, F. Evers, Single molecule magnetoresistance with combined antiferromagnetic and ferromagnetic electrodes, Nano Lett. 12 (10) (2012) 5131–5136, https://doi.org/10.1021/nl301967t.
[54] H. Seki, K. Nawa, C. Mitsumata, T.K. Yamada, Tuning epitaxial growth of atomically thin MnTe films on Fe(001) for creating van Der Waals 2D magnets, ACS Appl. Nano Mater. 8 (31) (2025) 15662–15672, https://doi.org/10.1021/acsanm.5c02678.
[55] J.A. Stroscio, D.T. Pierce, A. Davies, R.J. Celotta, M. Weinert, Tunneling spectroscopy of bcc (001) surface states, Phys. Rev. Lett. 75 (16) (1995) 2960–2963, https://doi.org/10.1103/PhysRevLett.75.2960.
[56] Y. Kosuge, T.K. Yamada, Spin-polarized scanning tunneling microscopy study of non-collinear magnetic coupling in layerwise antiferromagnetic Mn(001) ultra-thin films on Fe(001) due to interface roughening, Vac. Surf. Sci. 63 (9) (2020) 459–464, https://doi.org/10.1380/vss.63.459.
[57] U. Schlickum, N. Janke-Gilman, W. Wulfhekel, J. Kirschner, Step-induced frustration of antiferromagnetic order in Mn on Fe(001), Phys. Rev. Lett. 92 (10) (2004) 107203, https://doi.org/10.1103/PhysRevLett.92.107203.
[58] A. Cattoni, D. Petti, S. Brivio, M. Cantoni, R. Bertacco, F. Ciccacci, MgO/Fe(001) and MgO /Fe (001) − p (1 × 1) O interfaces for magnetic tunnel junctions: a comparative study, Phys. Rev. B 80 (10) (2009) 104437, https://doi.org/10.1103/PhysRevB.80.104437.
[59] T.K. Yamada, Y. Sakaguchi, L. Gerhard, W. Wulfhekel, Temperature control of the growth of iron oxide nanoislands on Fe(001), Jpn. J. Appl. Phys. 55 (8S1) (2016), https://doi.org/10.7567/JJAP.55.08NB14, 08NB14.
[60] F. Donati, P. Sessi, S. Achilli, A. Li Bassi, M. Passoni, C.S. Casari, C.E. Bottani, A. Brambilla, A. Picone, M. Finazzi, L. Duò, M.I. Trioni, F. Ciccacci, Scanning tunneling spectroscopy of the Fe (001) − p (1 × 1) O surface, Phys. Rev. B 79 (19) (2009) 195430, https://doi.org/10.1103/PhysRevB.79.195430.
[61] W. Kohn, L.J. Sham, Self-consistent equations including exchange and correlation effects, Phys. Rev. 140 (4A) (1965) A1133–A1138, https://doi.org/10.1103/PhysRev.140.A1133.
[62] J.P. Perdew, K. Burke, M. Ernzerhof, Generalized gradient approximation made simple, Phys. Rev. Lett. 77 (18) (1996) 3865–3868, https://doi.org/10.1103/PhysRevLett.77.3865.
[63] P.E. Blöchl, Projector augmented-wave method, Phys. Rev. B 50 (24) (1994) 17953–17979, https://doi.org/10.1103/PhysRevB.50.17953.
[64] G. Kresse, D. Joubert, From Ultrasoft pseudopotentials to the projector augmented-wave method, Phys. Rev. B 59 (3) (1999) 1758–1775, https://doi.org/10.1103/PhysRevB.59.1758.
[65] G. Kresse, J. Hafner, Ab initio molecular dynamics for liquid metals, Phys. Rev. B 47 (1) (1993) 558–561, https://doi.org/10.1103/PhysRevB.47.558.
[66] G. Kresse, J. Hafner, Ab initio molecular-dynamics simulation of the liquid-metal–Amorphous-semiconductor transition in Germanium, Phys. Rev. B 49 (20) (1994) 14251–14269, https://doi.org/10.1103/PhysRevB.49.14251.
[67] G. Kresse, J. Furthmüller, Efficient iterative schemes for ab initio total-energy calculations using a plane-wave basis set, Phys. Rev. B 54 (16) (1996) 11169–11186, https://doi.org/10.1103/PhysRevB.54.11169.
[68] G. Kresse, J. Furthmüller, Efficiency of ab-initio total energy calculations for metals and semiconductors using a plane-wave basis set, Comput. Mater. Sci. 6 (1) (1996) 15–50, https://doi.org/10.1016/0927-0256(96)00008-0.
[69] K. Momma, F. Izumi, VESTA 3 for three-dimensional visualization of crystal, volumetric and morphology data, J. Appl. Crystallogr. 44 (6) (2011) 1272–1276, https://doi.org/10.1107/S0021889811038970.

[70] G. Henkelman, A. Arnaldsson, H. Jónsson, A fast and robust algorithm for bader decomposition of charge density, Comput. Mater. Sci. 36 (3) (2006) 354–360, https://doi.org/10.1016/j.commatsci.2005.04.010.
[71] E. Sanville, S.D. Kenny, R. Smith, G. Henkelman, Improved grid-based algorithm for Bader charge allocation, J. Comput. Chem. 28 (5) (2007) 899–908, https://doi.org/10.1002/jcc.20575.
[72] W. Tang, E. Sanville, G. Henkelman, A grid-based bader analysis algorithm without lattice bias, J. Phys. Condens. Matter 21 (8) (2009) 084204, https://doi.org/10.1088/0953-8984/21/8/084204.
[73] M. Yu, D.R. Trinkle, Accurate and efficient algorithm for Bader Charge integration, J. Chem. Phys. 134 (6) (2011) 064111, https://doi.org/10.1063/1.3553716.
[74] M. Klaua, D. Ullmann, J. Barthel, W. Wulfhekel, J. Kirschner, R. Urban, T. L. Monchesky, A. Enders, J.F. Cochran, B. Heinrich, Growth, structure, electronic, and magnetic properties of MgO/Fe(001) bilayers and Fe/MgO/Fe(001) trilayers, Phys. Rev. B 64 (13) (2001) 134411, https://doi.org/10.1103/PhysRevB.64.134411.
[75] O. Dugerjav, H. Kim, J.M. Seo, Growth of a crystalline and ultrathin MgO film on Fe(001), AIP Adv 1 (3) (2011) 032156, https://doi.org/10.1063/1.3642601.
[76] J. Repp, G. Meyer, F.E. Olsson, M. Persson, Controlling the charge state of individual gold adatoms, Science 305 (5683) (2004) 493–495, https://doi.org/10.1126/science.1099557.
[77] K. Tada, K. Masuda, R. Kishi, Y. Kitagawa, Systematic investigation on surface diradicals using theoretical models: 2M/MgO and 2M/BaO (M = Cu, Ag, and Au), Chemistry (Easton) 6 (6) (2024) 1572–1592, https://doi.org/10.3390/chemistry6060095.
[78] Kh.M. Eid, H.O. Taha, M.A. Kamel, A.E. Ashour, W.S. Abdel Halim, DFT calculations of the CO adsorption on Mn, Fe, Co, and Au deposited at MgO (100) and CdO (100), Appl. Surf. Sci. 258 (24) (2012) 9876–9890, https://doi.org/10.1016/j.apsusc.2012.06.045.
[79] S. Tosoni, G. Pacchioni, Magnetic nature and hyperfine interactions of transition metal atoms adsorbed on ultrathin insulating films: a challenge for DFT, Phys. Chem. Chem. Phys. 24 (26) (2022) 15891–15903, https://doi.org/10.1039/D2CP01224C.
[80] V.A. Ukraintsev, Data evaluation technique for electron-tunneling spectroscopy, Phys. Rev. B 53 (16) (1996) 11176–11185, https://doi.org/10.1103/PhysRevB.53.11176.
[81] B.J. Van Wees, H. Van Houten, C.W.J. Beenakker, J.G. Williamson, L. P. Kouwenhoven, D. Van Der Marel, C.T. Foxon, Quantized conductance of point contacts in a two-dimensional electron gas, Phys. Rev. Lett. 60 (9) (1988) 848–850, https://doi.org/10.1103/PhysRevLett.60.848.
[82] E. Inami, P. Krüger, H. Hayashi, T.K. Yamada, Emergence of robust 1D atomic and electronic textures in Mn ultrathin films via antiferromagnet-ferromagnet interfaces, Small (2025) e04791, https://doi.org/10.1002/smll.202504791.
[83] T. Ossowski, A. Kiejna, Structure and energetics of FeO/Fe(001) interfaces, J. Phys. Condens. Matter. 35 (46) (2023) 465001, https://doi.org/10.1088/1361-648X/acede2.
[84] N.K.M. Nazriq, E. Minamitani, T.K. Yamada, CO-tip manipulation using repulsive interactions, Nanotechnology 29 (49) (2018) 495701, https://doi.org/10.1088/1361-6528/aae0df.
[85] L. Gerhard, T.K. Yamada, T. Balashov, A.F. Takacs, R.J.H. Wesselink, M. Dane, M. Fechner, S. Ostanin, A. Ernst, I. Mertig, W. Wulfhekel, Electrical control of the magnetic State of Fe, IEEE Trans. Magn. 47 (6) (2011) 1619–1622, https://doi.org/10.1109/TMAG.2011.2107506.
[86] S.W. Wu, G.V. Nazin, X. Chen, X.H. Qiu, W. Ho, Control of relative tunneling rates in single molecule bipolar electron transport, Phys. Rev. Lett. 93 (23) (2004) 236802, https://doi.org/10.1103/PhysRevLett.93.236802.
[87] P. Myrach, N. Nilius, H.-J. Freund, Photon mapping of individual Ag particles on MgO/Mo(001), Phys. Rev. B 83 (3) (2011) 035416, https://doi.org/10.1103/PhysRevB.83.035416.
[88] L. Yan, C.M. Lopez, R.P. Shrestha, E.A. Irene, A.A. Suvorova, M. Saunders, Magnesium oxide as a candidate high-κ gate dielectric, Appl. Phys. Lett. 88 (14) (2006) 142901, https://doi.org/10.1063/1.2191419.